Sphingolipid imbalance aggravates fibrillar Tau-induced endomembrane rigidification and rupture

Jessica Tittelmeier[1], Carl Alexander Sandhof[2,3], Nicole Martin[1], Deike El-Kabarity[1], Soki-Bradel Ngonza-Nito[4], Ronald Melki[4] and Carmen Nussbaum-Krammer[1,2,*]

[1]Chair of Neuroanatomy, Institute of Anatomy, Faculty of Medicine, Ludwig-Maximilians University of Munich (LMU), Pettenkoferstrasse 11, 80336 Munich, Germany

[2]Center for Molecular Biology of Heidelberg University (ZMBH) and German Cancer Research Center (DKFZ), DKFZ-ZMBH Alliance, Im Neuenheimer Feld 282, 69120 Heidelberg, Germany

[3]Chemical Neurobiology Laboratory, Center for Genomic Medicine, Departments of Neurology and Psychiatry, Massachusetts General Hospital and Harvard Medical School, Boston, MA 02114, USA

[4]Institute Francois Jacob (MIRCen), CEA, and Laboratory of Neurodegenerative Diseases, CNRS, Fontenay-Aux-Roses, France

*Correspondence should be addressed to carmen.nussbaum@med.uni-muenchen.de

Abstract

Numerous studies have implicated endolysosomal dysfunction in Alzheimer's disease (AD) and related tauopathies. However, the mechanisms driving these disturbances remain poorly understood. Using *C. elegans*, we recently identified genes involved in sphingolipid metabolism as crucial for the maintenance of endolysosomal integrity. Abnormal sphingolipid metabolism is increasingly reported in AD, but its impact on Tau pathology remains unclear. Here, we investigated the role of sphingolipid metabolism in endolysosomal membrane homeostasis and its effect on Tau aggregation and toxicity in *C. elegans* and human cell culture models. Fluorescence recovery after photobleaching (FRAP) analysis and C-Laurdan dye imaging revealed that silencing of sphingolipid metabolism genes reduced the fluidity of endolysosomal vesicle membranes, and increased their susceptibility to rupture. The accumulation of aggregated Tau in endolysosomal vesicles further exacerbated endomembrane rigidification and damage. Moreover, enhanced membrane rigidity facilitated seeded Tau aggregation in a biosensor cell line. Restoring membrane fluidity by supplementation with the polyunsaturated omega-3 fatty acid alpha-linoleic acid suppressed endomembrane rupture and seeded Tau aggregation in cell models and neurotoxicity in *C. elegans*. This study provides mechanistic insights into how impaired sphingolipid homeostasis leads to endolysosomal membrane damage and how this might contribute to the progression of tau pathology.

Keywords: Alzheimer's disease, Tau propagation, sphingolipid metabolism, endolysosomal system, lipid homeostasis

Introduction

The gradual accumulation of an abnormally folded, aggregated form of the microtubule-associated protein Tau (MAPT/Tau) is a hallmark of Alzheimer's disease (AD) and related tauopathies. Misfolded Tau proteins exhibit prion-like behavior by self-replicating and spreading from cell to cell[1]. This contributes to the progression of pathology and neurotoxicity, eventually culminating in widespread neuronal dysfunction and degeneration[2]. At the molecular level, pathological Tau species replicate by templating the conversion of native Tau into an amyloid conformation, promoting its accumulation into fibrillar aggregates. For this to occur at the cellular level, seeding-competent Tau species (or "Tau seeds") must eventually be secreted from a cell and taken up into the cytosol of the neighboring cell in order to come into direct contact with the cytosolic native Tau protein.

In this process, the autophagy-lysosomal pathway (ALP), which is an important clearance route for Tau[3], appears to play a central role. Studies have demonstrated impaired ALP function in the brains of tauopathy patients as well as in animal and cell models, showing that the accumulation of abnormal autolysosomal and endolysosomal vesicles correlating with neuronal toxicity[4–6]. It is still unclear whether impaired autophagy contributes to or is a consequence of tauopathy, but it affects the intercellular propagation of Tau in several ways. For one, inhibition of autophagic clearance of Tau increases its secretion and spreading[7]. In addition, the accumulation of misfolded Tau within endolysosomes leads to a destabilization and rupture of these vesicles[8–10]. The escape of Tau seeds from the endolysosomal system to the cytosol has recently emerged as a crucial rate-limiting event in seeded Tau propagation[8–10].

To identify cellular factors that are critical for the integrity of endolysosomal vesicles, we recently performed an unbiased genome-wide RNAi screen[11]. We used a new *C. elegans* model for Tau spreading that expresses an aggregation-prone fragment of human Tau labeled with mCherry ($F3^{\Delta K281}$::mCherry) in the six touch receptor neurons[11]. $F3^{\Delta K281}$::mCherry spreads from these neurons to the neighboring hypodermis, compromising the endolysosomal system[11]. The RNAi screen identified genes whose knockdown causes endolysosomal rupture in the receiving hypodermal tissue[11]. One of the pathways identified was sphingolipid (SL) metabolism.

SLs constitute a large and diverse class of lipids that are involved in various physiological processes[12]. They consist of two main building blocks, a long-chain base with a serine backbone and an attached long acyl chain. This characteristic chemical structure mediates unique biophysical

78 properties. SL biosynthesis and degradation rely on a specialized enzymatic machinery distinct
79 from that of other lipids[13] (Fig. 1a). Functionally, SLs, along with glycerolipids and sterols, serve
80 as structural components of cell membranes, contributing to the stability and fluidity of membranes
81 and to the organization of microdomains such as lipid rafts. Beyond their structural role, SLs serve
82 as bioactive molecules participating in cellular signaling pathways that control cell growth,
83 differentiation, apoptosis, and intercellular communication. Consequently, their dysregulation has
84 been implicated in various diseases, including metabolic disorders and cancer, due to altered
85 cellular signaling and membrane properties. Abnormalities in SL metabolism have also been
86 observed during aging and in neurodegenerative conditions, including AD, underscoring their
87 potential significance in the pathogenesis of these disorders[14,15].
88 Here we investigated the role of SL metabolism in the maintenance of endolysosomal
89 vesicle integrity. Our results revealed that silencing of SL metabolism genes led to a marked
90 reduction in membrane fluidity, particularly in endolysosomal vesicles, thereby increasing their
91 fragility and rupture. Accumulation of aggregated Tau further disrupted endolysosomal membrane
92 dynamics, increasing membrane rigidity and exacerbating damage to the endolysosomal
93 compartment. Notably, the increased membrane rigidity facilitated seeded Tau aggregation in a
94 biosensor cell line. Improvement of membrane fluidity through supplementation of
95 polyunsaturated fatty acids (PUFAs) counteracted Tau propagation in cells and Tau-associated
96 neurotoxicity in *C. elegans*. Overall, this study emphasizes the importance of membrane
97 homeostasis in neurodegenerative disease progression and provides a possible mechanism for the
98 beneficial effect of PUFA supplementation that has been observed in AD patients.
99

100 **Results**

101 **Knockdown of sphingolipid metabolism genes induces lysosomal rupture**

102 Several of the strongest hits identified in the unbiased genome-wide RNAi screen we
103 performed to identify modulators of endolysosomal vesicles integrity were genes involved in SL
104 metabolism (Fig.1a). Knockdown (KD) of these genes (the serine incorporator *R11H6.2*, the 3-
105 ketodihydrosphingosine reductase *Y37E11AM.3,* the hydroxyacyl-CoA dehydratase *hpo-8*, the
106 cytochrome b5 reductases *hpo-19* and *T05H4.4,* the saposin *spp-10*, the sphingosine kinase *sphk-*
107 *1*, and the sphingosine-1-phosphate lyase *spl-1*) via RNA interference (RNAi) induced
108 endolysosomal membrane damage as detected by a galectin puncta assay[16] (Fig.1b-d). Under
109 steady-state conditions, human galectin-3 fused to superfolder-GFP (sfGFP::LGALS3) exhibits an
110 even distribution within the cytosol of hypodermal cells. Upon endolysosomal vesicle damage and
111 exposure of their lumen to the cytosol, sfGFP::LGALS3 binds exposed β-galactoside and re-
112 localizes, yielding visible puncta[16].

113 The screen identified distinct steps in sphingolipid metabolism catalyzed by non-redundant
114 genes or targeted by a single RNAi clone, as in the case of *hpo-19*/*T05H4.4* which are both
115 depleted by *hpo-19* RNAi. However, other steps in this pathway, which are mediated by two or
116 more proteins[17], may have been missed in the screen. Indeed, simultaneous KD of selective
117 redundant genes using co-RNAi revealed additional genes functioning in *de novo* sphingolipid
118 biosynthesis that also induced endolysosomal rupture, including the serine palmitoyltransferases
119 *sptl-1* and *-3* and the ceramide synthases *hyl-1* and *-2* (Supplementary Fig.1a). In addition, the co-
120 KD of all four glucocerebrosidases *gba-1-4* or only *gba-2-4*, also triggered endolysosomal rupture
121 (Supplementary Fig.1b). Hence, these findings suggest that the KD of genes involved in both
122 biosynthesis and degradation of SLs contributes to endolysosomal rupture, highlighting the tightly
123 regulated nature of sphingolipid metabolism. Any disruption in this balance poses challenges to
124 endolysosomal integrity.

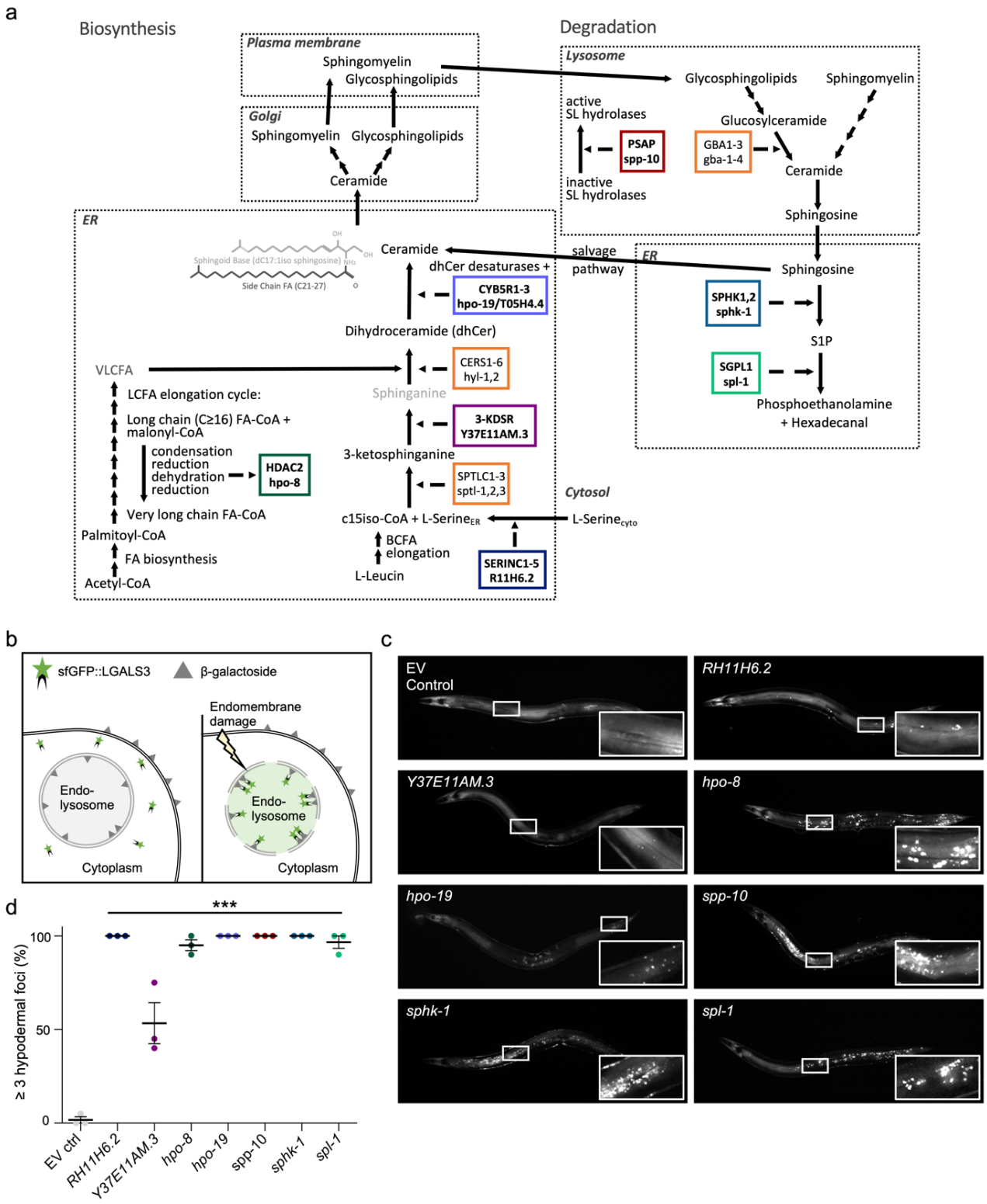

Figure 1: Sphingolipid metabolism dysregulation by KD is linked to of endolysosomal vesicle rupture. **a** General overview of sphingolipid metabolism with a particular focus on the genes identified in the screen we performed. Sphingolipids constitute a group of amphipathic lipids featuring a polar head group and a sphingoid base backbone that is N-acetylated with a (very) long-chain fatty acid ((V)LCFA) side chain. In

contrast to mammals, where the sphingoid base is conventionally derived from palmitic acid and serine, *C. elegans* sphingolipids usually contain a characteristic C17iso branched chain sphingoid base[54–56]. Its synthesis involves the branched chain FA (BCFA) elongation pathway to yield C15iso-CoA, which then condensates with L-serine to form 3-ketosphinganine. This reaction is catalyzed by serine palmitoyltransferase (encoded by *sptl-1*, *-2*, and *-3*). The serine incorporator (SERINC) protein family (encoded by *R11H6.2*) is believed to assist in the incorporation of L-serine into specific membranes. 3-ketodihydrosphingosine reductase (KDSR, in *C. elegans* predicted to be encoded by Y37E11AM.3) then catalyzes the reduction of 3-keto sphinganine to sphinganine. The (V)LCFA side chain is primarily comprised of a straight saturated FA chain, ranching from 20-26 carbon atoms in length, with or without hydroxylation[18,57]. It can be also derived from BCFAs, such as C15iso and C17iso[54,55]. However, most of the side chain FA moieties originate from palmitoyl-CoA via the canonical de novo FA biosynthesis pathway, involving the sequential addition of C2 moieties from malonyl-CoA through the LCFA elongation cycle[54,55]. Each elongation cycle comprises four reactions (condensation, reduction, dehydration, reduction), with the third reaction requiring very-long-chain (3R)-3-hydroxyacyl-CoA dehydratase (encoded by *hpo-8*)[55]. Finally, ceramide synthases (encoded by *hyl-1* and *hyl-2*) catalyze the addition of various acyl side chains to the sphingoid base to yield dihydroceramide, which is then desaturated to ceramide. The latter reaction is catalyzed by dihydroceramide desaturases, which require electrons from NAD(P)H provided by cytochrome b5 reductases (encoded by *hpo-19* and *T05H4.4*). All complex sphingolipids, such as sphingomyelin and glycosphingolipids (including cerebrosides and gangliosides) originate from ceramide. Degradation of complex sphingolipids takes place in the lysosome. Essential for this process are saposins or sphingolipid activator proteins (PSAPs, encoded by *spp-10*), which serve as crucial bridges between the lipid substrate and hydrophilic hydrolases. Glucocerebrosidases (encoded by *gba-1*, *gba-2*, *gba-3*, and *gba-4*) hydrolyse glucosylceramide into ceramide and glucose. Sphingosine may be either recycled and metabolized back into ceramide or phosphorylated by sphingosine kinase (encoded by *sphk-1*) to generate sphingosine-1-phosphate (S1P). S1P lyase (encoded by *spl-1*) irreversibly cleaves S1P into phospho-ethanolamine and hexadecenal. The *C. elegans* genes identified in the primary screen, along with their human orthologs, are framed with color. Genes identified in subsequent co-RNAi experiments and their human orthologs are framed in gray. **b** Schematic of lysosomal rupture detected by the galectin puncta assay. **c** Widefield fluorescence images of animals expressing hypodermal sfGFP::LGALS3. Numerous foci are visible upon RNAi-mediated KD of sphingolipid metabolisms genes. Zoomed in image is indicated in overview image by a white box. **d** Mean percentage of animals positive for lysosomal rupture (defined as three or more sfGFP::LGALS3 foci in the hypodermis). Data shown as means of three technical replicate plates with 17-30 animals per plate ± SEM. Statistical analysis comparing RNAi conditions to the empty vector control (EV ctrl) was done using one-way ANOVA with Dunnett's post-hoc test. *** = $p < 0.001$.

KD of sphingolipid metabolism genes particularly affects membrane fluidity of endolysosomal vesicles

SLs are important components of eukaryotic cell membranes and genetic modulation of SL metabolism likely affects the lipid composition and biophysical properties of membranes. Similar to their mammalian isoforms, the N-acyl chains of *C. elegans* SLs contain predominantly long and saturated fatty acid chains[18,19], which tend to pack tightly within the lipid bilayer. As such, a higher

172 proportion of SLs generally reduces membrane fluidity, leading to increased order, rigidity, or
173 viscosity[20]. Consequently, KD of the hits involved in SL degradation should lead to SL
174 accumulation and reduced membrane fluidity, while KD of the hits involved in SL biosynthesis
175 should have the opposite effect.

176 To evaluate the membrane fluidity of endolysosomal membranes, fluorescence recovery
177 after photobleaching (FRAP) was employed on *C. elegans* that express the Lysine/Arginine
178 Transporter 1 (LAAT-1) tagged with mCherry, which localizes to the lysosomal membrane[21].
179 FRAP enables the assessment of the lateral mobility of LAAT-1 within the lysosomal membrane,
180 thereby indirectly measuring its fluidity. We focused our analysis on the hypodermis, where we
181 expressed the sfGFP::LGALS3 reporter and observed endolysosomal rupture following KD of the
182 SL metabolism genes (Fig.1c, d). Interestingly, KD of all of our hits significantly increased the
183 time required to recover half of the maximum fluorescence intensity (t_{half}), indicating less fluid
184 lysosomal membrane in the hypodermis (Fig.2a-c, e, f). With some gene KDs, we also observed a
185 decrease in the maximal recovered signal after bleaching (Figure 2d, 2g). The decrease in
186 lysosomal membrane fluidity was not specific to the hypodermis as the KD of *spl-1* also increased
187 the t_{half} of LAAT-1::mCherry in intestinal lysosomes (Supplementary Fig.2a-d). To discern
188 whether the detrimental effect of KD on membrane fluidity is confined to lysosomal membranes
189 or extends to other cellular membranes, we utilized a *C. elegans* strain expressing a plasma
190 membrane-anchored GFP[22]. Intriguingly, this reporter showed no change in the t_{half} with any KD
191 and only *spl-1* KD led to decrease in the maximal recovered signal (Fig.2h-k). Hence, the
192 endolysosomal membrane seems to be particularly sensitive to a disruption of SL metabolism in
193 contrast to the plasma membrane. Dysregulation of both, synthesis and degradation of SLs reduces
194 the fluidity of the endolysosomal membrane and makes it more susceptible to rupture.

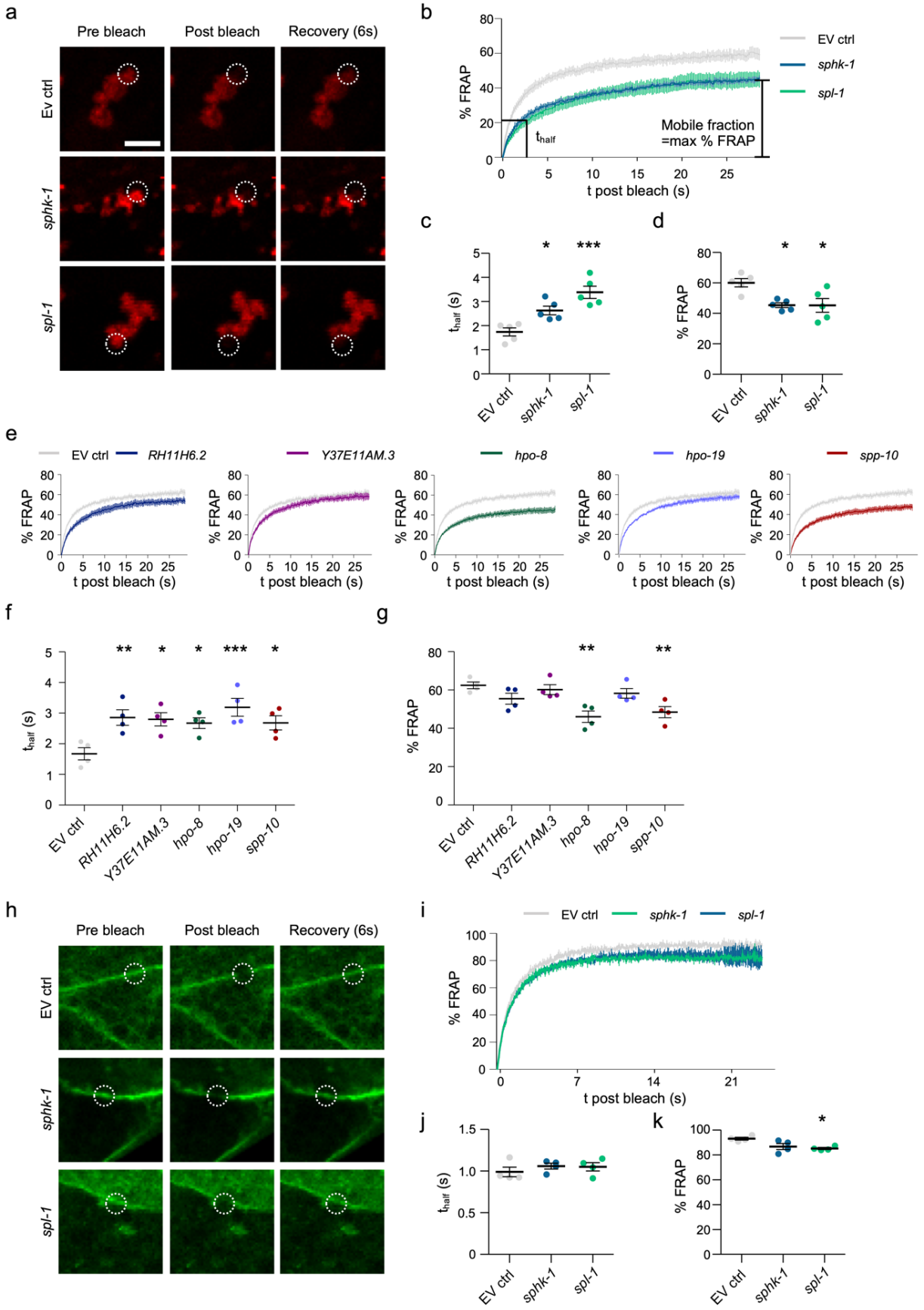
a
Pre bleach
Post bleach
Recovery (6s)
Ev ctrl
sphk-1
spl-1
b
% FRAP
t post bleach (s)
EV ctrl
sphk-1
spl-1
t_{half}
Mobile fraction
=max % FRAP
c
t_{half} (s)
d
% FRAP
e
EV ctrl
RH11H6.2
Y37E11AM.3
hpo-8
hpo-19
spp-10
f
t_{half} (s)
g
% FRAP
h
Pre bleach
Post bleach
Recovery (6s)
EV ctrl
sphk-1
spl-1
i
% FRAP
t post bleach (s)
j
t_{half} (s)
k
% FRAP

196 **Figure 2: Knockdown of genes involved in sphingolipid metabolism decreases lysosomal membrane**
197 **fluidity.**
198 **a** Representative confocal single plane images from a FRAP experiment in animals expressing a mCherry
199 tagged Lysosomal Lysine/Arginine Transporter 1 (LAAT-1::mCherry) in the hypodermis grown either on
200 empty vector control (EV ctrl), *spl-1* or *sphk-1* RNAi plates. Dashed circles outline the bleach spots. **b**
201 Combined FRAP curves of LAAT-1::mCherry in hypodermal lysosomal membranes. Curves are
202 normalized to the pre-bleach intensity as 100% and the first post-bleach intensity as 0%. **c** Increase in the
203 mean time until half of the maximal signal is recovered (t_{half},) and **d** decrease in the maximal % recoverable
204 fluorescence values upon KD of *sphk-1* and *spl-1* indicate a reduction in lysosomal membrane fluidity. **e**
205 FRAP curves of LAAT-1::mCherry in hypodermal lysosomal membranes of animals grown either on empty
206 vector or the indicated RNAi plates. Curves are normalized to the pre-bleach intensity set as 100% and the
207 first post-bleach intensity as 0%. **f** Mean t_{half} upon KD of sphingolipid metabolism genes. **g** Maximal %
208 recoverable fluorescence values upon KD of sphingolipid metabolism genes. **h** Representative confocal
209 single plane images from a FRAP experiment in animals expressing prenylated GFP for lipid membrane
210 anchorage in the intestine. **i** Combined FRAP curves of prenylated GFP enriched on the intestinal plasma
211 membrane of animals grown either on empty vector, *sphk-1* or *spl-1* RNAi plates. Curves are normalized
212 to the pre-bleach intensity as 100% and the first post-bleach intensity as 0%. **j** Mean t_{half} and **k** maximal %
213 recoverable fluorescence values. Data represented as means ± SEM of 5 – 12 FRAP measurements per
214 condition collected in five biological replicates. Statistical analysis comparing RNAi conditions to the
215 empty vector control was done using one-way ANOVA with Dunnett's post-hoc test. n.s.: not significant,
216 * = $p < 0.05$, ** = $p < 0.01$, *** = $p < 0.001$
217

218 **KD of sphingolipid metabolism genes affects membrane fluidity in human cells**

219 Next, we asked whether dysregulation of SL metabolism exerts similar effects in human
220 cells. To this end, we employed HEK293T cells and C-Laurdan dye to evaluate membrane fluidity
221 (Fig.3a). This approach leverages the unique properties of C-Laurdan, which emits fluorescent
222 light of varying wavelengths in response to changes within the phospholipid bilayer, particularly
223 reflective of membrane fluidity[23,24]. The shift in emission profile between liquid-disordered and
224 liquid-ordered phases allows a quantitative assessment of the membrane order by calculating the
225 ratiometric relationship of the fluorescence intensity recorded in two spectral channels, known as
226 a generalized polarization (GP) value[23] (Fig.3a). Decreasing GP values are indicative of
227 increasingly fluid membrane while increasing GP values denote increased rigidity. Of note, we
228 exposed the cells to C-Laurdan for an extended time of 2 hours (instead of 30 min as recommended
229 in the original protocol), to promote internalization of the dye and thus increase the staining of
230 endolysosomal membranes relative to the plasma membrane[23]. Upon KD of *SPHK2*, one of the
231 human homologs of the *C. elegans sphk-1* gene, the C-Laurdan fluorescence GP ratio augmented
232 significantly, indicating increased membrane rigidity (Fig.3b, c and Supplementary Fig.3a). Of
233 note, Lipofectamine 2000 was used to deliver siRNA into the cells and lipid-based transfection

234 reagents have been shown to impact endolysosomal membranes[25]. Indeed, Lipofectamine alone
235 slightly increased membrane fluidity (Fig.3c). Taken together, FRAP and C-Laurdan analyses
236 revealed that disrupted SL homeostasis led to more ordered and rigid endolysosomal membranes,
237 in both *C. elegans* and human cells.
238
239 **Fibrillar Tau increases membrane rigidity and exacerbates endolysosomal damage**
240 To investigate whether disruption of SL homeostasis also affects endolysosomal integrity in
241 human cells, we generated a HEK293T cell line stably expressing the same sfGFP-LGALS3
242 reporter used for the galectin puncta assay in *C. elegans*. To further mimic the *C. elegans* model,
243 in which aggregation-prone Tau fragments are chronically transferred from the touch receptor
244 neurons into the hypodermis where the sfGFP-LGALS3 reporter is expressed[11], recombinant
245 1N4R Tau fibrils were added to sfGFP-LGALS3 expressing HEK293T cells on top of the KD of
246 *SPHK2*. Interestingly, both the addition of Tau fibrils alone and the KD of *SPHK2* alone already
247 caused rupture of endolysosomes in sfGFP-LGALS3 cells (Fig.3d, e and Supplementary Fig.3b).
248 The combination of both had an additive effect (Fig.3d, e and Supplementary Fig.3b).
249 We therefore asked whether the KD of SLs alone would also already rupture hypodermal
250 endolysosomes in *C. elegans* and whether accumulation of transmitted Tau would exacerbate this
251 process. To answer this question, we determined the amount of hypodermal sfGFP-LGALS3 foci
252 in F3$^{\Delta K281}$::mCherry *C. elegans* compared to control animals expressing only the mCherry tag. KD
253 of *Y37E11AM.3* alone did not increase lysosomal rupture compared to the EV control RNAi, only
254 the presence of Tau spreading resulted in more lysosomal rupture relative to the control (Fig.3f).
255 KD of the remaining hits resulted in near 100% animals with hypodermal sfGFP-LGALS3 foci in
256 both the F3$^{\Delta K281}$::mCherry and mCherry control strains. To test whether the additional negative
257 impact of the F3 Tau fragment might be masked by the strength of the RNAi clones, different
258 dilutions of the RNAi bacteria were tested. Under conditions where the RNAi KD did not saturate
259 the readout of the assay, KD of *spl-1, hpo-8,* and *hpo-19* alone already affected lysosomal integrity
260 (Fig.3g). Moreover, F3$^{\Delta K281}$::mCherry transgenic animals showed a significantly higher level of
261 endolysosomal rupture upon KD of *spl-1, hpo-8,* and *hpo-19* compared to the mCherry control
262 (Fig.3g). Diluting the *R11H6.2* RNAi clone showed no significant differences, and KD of *sphk-1*
263 still resulted in 100% endolysosomal rupture-positive animals in both genetic backgrounds even
264 after dilution of the RNAi bacteria to below 5% and could therefore not be assessed. In conclusion,

265 chronic transmission of the $F3^{\Delta K281}$::mCherry fragment from the touch receptor neurons to the
266 hypodermis impaired the endolysosomal system exacerbating the rupture due to perturbation of
267 SL homeostasis.

268 Since disruption of SLs metabolism led to an increase in membrane rigidity resulting in
269 endolysosomal rupture, and fibrillar Tau also ruptured endolysosomal membranes (Fig.3d, e)[9], we
270 asked whether Tau itself could also affect membrane fluidity. To test this, membrane fluidity was
271 assessed for somas of the posterior (PLM) touch receptor neurons of *C. elegans* using C-Laurdan
272 dye. Indeed, expression of the Tau fragment led to a decrease in membrane fluidity compared to
273 expression of the mCherry tag alone (Fig.3h, i). Also, HEK293T cells incubated with Tau fibrils
274 for 5 hours exhibited an increased GP index (Figure 3j, k). Importantly, this was specific to fibrillar
275 Tau, as monomeric Tau had no effect on membrane fluidity (Fig.3l and Supplementary Fig.3c).
276 Thus, aggregated forms of Tau can cause rigidification of the endolysosomal membrane, resulting
277 in increased fragility and rupture.

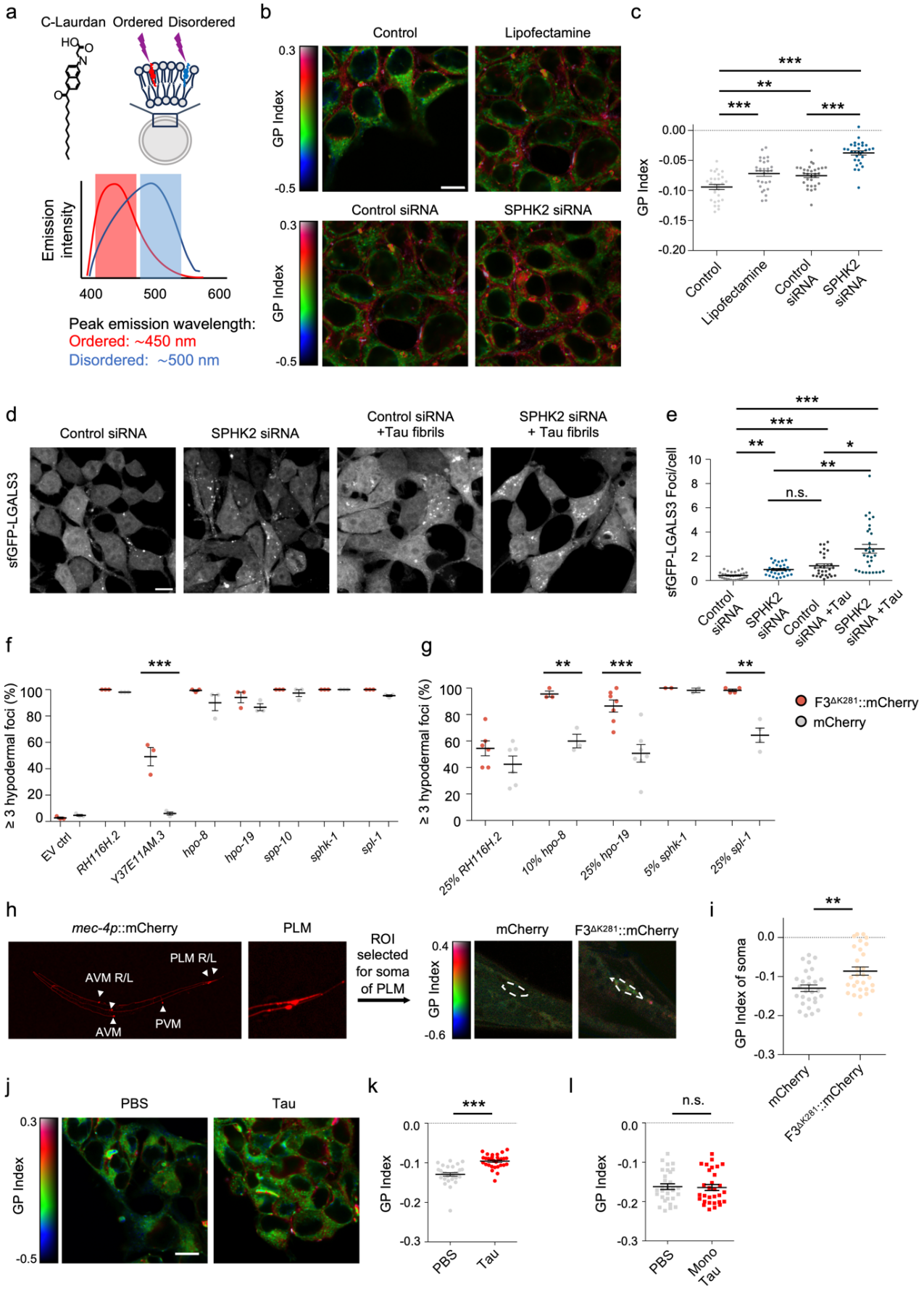
a
C-Laurdan
Ordered
Disordered
Emission intensity
400
500
600
Peak emission wavelength:
Ordered: ~450 nm
Disordered: ~500 nm
b
Control
Lipofectamine
Control siRNA
SPHK2 siRNA
GP Index
0.3
-0.5
c
GP Index
Control
Lipofectamine
Control siRNA
SPHK2 siRNA
d
Control siRNA
SPHK2 siRNA
Control siRNA +Tau fibrils
SPHK2 siRNA + Tau fibrils
sfGFP-LGALS3
e
sfGFP-LGALS3 Foci/cell
n.s.
Control siRNA
SPHK2 siRNA
Control siRNA +Tau
SPHK2 siRNA +Tau
f
≥ 3 hypodermal foci (%)
EV ctrl
RH116H.2
Y37E11AM.3
hpo-8
hpo-19
spp-10
sphk-1
spl-1
g
≥ 3 hypodermal foci (%)
25% RH116H.2
10% hpo-8
25% hpo-19
5% sphk-1
25% spl-1
F3ΔK281::mCherry
mCherry
h
mec-4p::mCherry
PLM
PLM R/L
AVM R/L
AVM
PVM
ROI selected for soma of PLM
mCherry
F3ΔK281::mCherry
GP Index
i
GP Index of soma
mCherry
F3ΔK281::mCherry
j
PBS
Tau
GP Index
k
GP Index
PBS
Tau
l
n.s.
GP Index
PBS
Mono Tau

Figure 3: KD of SPHK2 and aggregated Tau reduces membrane fluidity leading to lysosomal rupture
a Scheme of the fluorescence properties of C-Laurdan. The dye is excited using illumination at 405 nm. The dye fluoresces with a peak emission wavelength around 450 nm (red) when residing in the ordered phase and ~500 nm in the disordered phase (blue). Two-channel acquisition is conducted in the wavelength bands indicated by shaded boxes. **b** Pseudo-color images showing the GP index of C-Laurdan dye at each pixel position in HEK293T cells upon KD of SPHK2. **c** Increase in GP Index of HEK293T cells upon KD of SPHK2. Statistical analysis was done using one-way ANOVA with Bonferroni's post-hoc test. **d** Max. intensity projection of confocal z-stacks of HEK293T cells expressing sfGFP-LGALS3 upon KD of SPHK2 and seeding with 1N4R Tau fibrils. **e** Average number of foci per number of cells. n= 3 independent experiments, 10 images each. Statistical analysis done using oKruskal-Wallis with a Dunn's post-hoc test. **f** Quantification of the percentage of animals with ≥ 3 hypodermal sfGFP::LGALS3 foci, representing endolysosomal damage, expressing either the $F3^{\Delta K281}$::mCherry (red) or only the mCherry tag (grey) in touch receptor neurons under knockdown of the indicated genes. **g** Dilution of the indicated RNAi cultures with the empty vector control culture was done to reduce the strength of the knockdown. Data represented as mean ± SEM. Besides knockdown of *sphk-1* in **c** n = 3 - 7 with (F) 40 – 50 or (G) 20 – 30 animals per replicate. Since even a dilution down to 5% of the *sphk-1* RNAi resulted in 100% of animals being scored as positive in two independent replicates this condition was not repeated further. Statistical analysis comparing RNAi conditions to the empty vector control done using one-way ANOVA with Dunnett's post-hoc test. **h** Worms expressing $F3^{\Delta K281}$::mCherry or mCherry in touch receptor neurons stained with C-Laurdan. The mCherry signal was used to select a region of interest (ROI) around the soma of the posterior touch receptor neurons (PLM) to determine the GP Index. **i** Increase in rigidity of membranes in animals expressing $F3^{\Delta K281}$::mCherry compared to mCherry. Statistical analysis was done using a t-test. n=4, total of at least 28 worms. **j** Pseudocolored HEK293T cells exposed to Tau 1N4R fibrils visualizing the C-Laurdan dye GP Index. **k** Increase rigidity of membranes of cells seeded with Tau fibrils as indicated by the GP index. **l** GP index of cells seeded with monomeric Tau. Statistical analysis for C-Laurdan in cells was done using a t-test. n= 3 independent experiments, 10 images each. Scale bar 10 µm. n.s.: not significant, * = $p < 0.05$, ** = $p < 0.01$, *** = $p < 0.001$.

Membrane rigidification exacerbates seeded Tau aggregation

The packing of fatty acids within the membrane influences membrane fluidity. Saturated fatty acids (SFAs) have straight hydrocarbon chains forming a tightly packed, highly ordered and rigid membrane. To investigate the role endomembrane lipid homeostasis plays in Tau propagation, we introduced an SFA to rigidify membranes. Incubating HEK293T cells with the SFA palmitic acid (PA) conjugated to BSA increased membrane rigidity (Fig.4a, b). In addition, cells incubated with PA and Tau fibrils had an even more rigid membrane than cells incubated with Tau fibrils alone (Fig.4c, d).

An important step in Tau propagation is Tau seeds escape from the endolysosomal compartment, which can then propagate themself by recruiting native monomeric Tau. Therefore, we asked if the PA-induced loss of membrane fluidity impairs endolysosomal integrity. Worms

318 grown on plates supplemented with PA displayed an increase in endolysosomal rupture (Fig.4e).
319 In cells, the addition of PA alone did not lead to endolysosomal rupture; however due to
320 compounding impact of PA and Tau fibrils on membrane fluidity, the addition of PA increased
321 fibrillar Tau-induced endolysosomal rupture (Fig.4f, g). Hence, loss of membrane fluidity
322 mediated by fibrillar Tau and/or SFAs negatively affects endolysosomal integrity, resulting in
323 increased endolysosomal rupture.

324 Impairment of endolysosomal integrity may enhance Tau propagation as Tau could escape
325 from the endolysosomal compartments, reach the cytosol and recruit native monomeric Tau,
326 promoting seeded Tau aggregation. Given the observed membrane rigidification after pre-loading
327 with SFAs, we investigated whether membrane lipid composition influences Tau propagation
328 using a Tau biosensor cell line expressing Venus-tagged full-length P301S mutant 0N4R Tau (Tau-
329 Venus)[26,27]. PA-induced membrane rigidification led to an increase in Tau-Venus foci upon
330 seeding with Tau fibrils (Fig.4h, i). Moreover, KD of *SPHK2* also increased the formation of Tau-
331 Venus foci due to SPHK2 KD-mediated membrane rigidification (Supplementary Fig.4c, d). This
332 highlights a positive correlation between membrane rigidity and seeded Tau aggregation. Changes
333 in membrane fluidity, which compromise endolysosomal integrity may promote the entry of seeds
334 into the cytosol. This would consequently foster the seeded propagation of Tau aggregation.
335
336

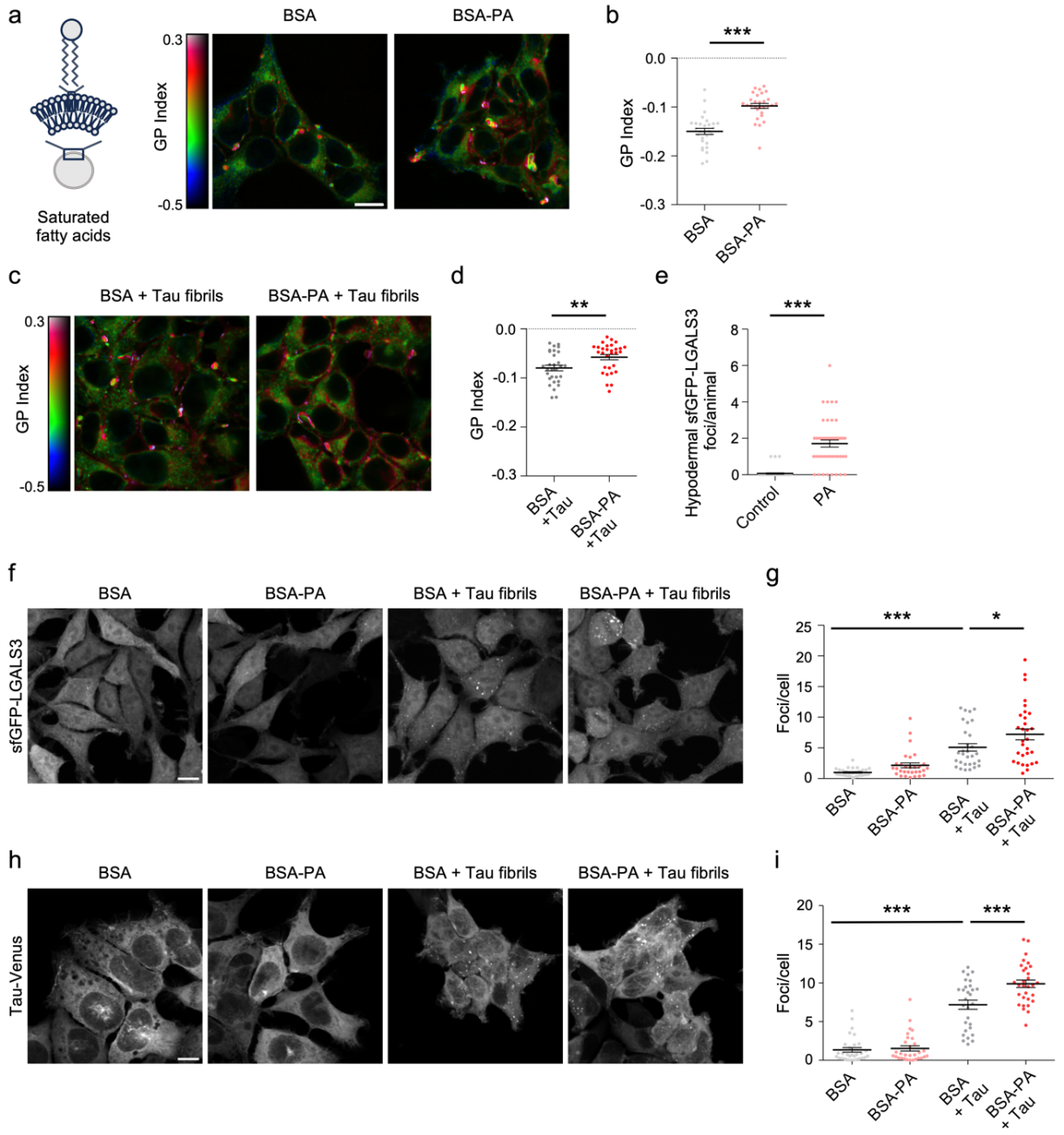

Figure 4: Saturated fatty acids decrease membrane fluidity and exacerbate seeded Tau aggregation **a** Left: saturated fatty acid membrane scheme. Right: pseudocolored HEK293T cells pre-loaded with 50 µM PA conjugated to BSA (BSA-PA) displaying the C-Laurdan dye GP Index. **b** GP Index indicates increased rigidity of membranes with BSA-PA. Statistical analysis was done using the Mann-Whitney-test. n= 3 independent experiments, 10 images each. **c** Pseudocolored HEK293T cells pre-loaded with BSA-PA and seeded with 1N4R Tau fibrils. **d** GP Index indicates an additive impact of Tau fibrils on membrane rigidity when added to HEK293T cells pre-loaded with BSA-PA. Statistical analysis was done using t-test. n= 3 independent experiments, 10 images each. **e** Quantification of hypodermal sfGFP-LGALS3 foci in animals grown on plates supplemented with PA reveal an increase in lysosomal rupture. Statistical analysis was done using Mann-Whitney test. n= 3 independent experiments, 15 worms per replicate. **f** Max.

intensity projection of confocal z-stacks of HEK293T cells expressing sfGFP-LGALS3 pre-loaded with BSA-PA and seeded with 1N4R Tau fibrils. **g** Quantification of sfGFP-LGALS3 foci in HEK293T cells following indicated treatments. **h** Max. intensity projection of confocal z-stacks of Venus-tagged full-length P301S Tau biosensor cells pre-loaded with BSA-PA and seeded with 1N4R Tau fibrils. **i** Quantification of Venus-P301S Tau foci following indicated treatments. Statistical analysis comparing BSA + Tau to other conditions was done using one-way ANOVA with Dunnett's post-hoc test. n= 3 independent experiments, 10 images each. * = $p < 0.05$, ** = $p < 0.01$, *** = $p < 0.001$. Scale bar 10 µm.

Increasing membrane fluidity by PUFAs rescues neurotoxic phenotypes

Given that membrane stiffening exacerbates Tau propagation, we wondered whether we could prevent this by improving membrane viscosity. While SFA allow for tightly packed lipids, unsaturated fatty acids have one or more double bonds in their hydrocarbon chain that introduce kinks in their structure, resulting in loosely packed lipids and increased membrane fluidity. Therefore, we investigated whether we could rescue Tau pathology using polyunsaturated fatty acids (PUFAs). Incubating HEK293T cells with the ω-3 PUFA α-linolenic acid (ALA) increased membrane fluidity (Fig.5a and Supplementary Fig.5a). Moreover, pre-loading with ALA prevented Tau-induced membrane rigidification and decreased the GP-index of membranes even after the addition of Tau fibrils (Fig.5b, c). Importantly, pre-loading cells with ALA also counteracted fibrillar Tau-mediated endolysosomal rupture (Fig.5d, e and Supplementary Fig.5b).

Since ALA prevented endolysosomal rupture, we expected it to also prevent seeded Tau aggregation. Indeed, Tau-Venus cells pre-loaded with ALA exhibited significantly fewer foci when exposed to Tau fibrils (Fig.5f and Supplementary Fig.5c). These data show that ALA supplementation counteracts Tau-mediated decrease in membrane fluidity, thereby preventing endolysosomal rupture and decreasing seeded Tau aggregation.

Finally, we asked whether ALA would also reduce the toxicity associated with aggregated Tau. Expression of $F3^{\Delta K281}$::mCherry in touch receptor neurons resulted in an age-dependent decline in the response to gentle touch from day 4, corresponding to the first day of adulthood to day 8, corresponding to day 5 of adulthood (Fig.5h, and Supplementary Fig.5d)[11]. Addition of ALA to the growth medium mitigated this loss of function (Fig.5h and Supplementary Fig.5d) and also reduced neurotoxicity (Fig,5i, j). Thus, supplementation with ALA not only reduced endolysosomal damage but also attenuated neurotoxic phenotypes associated with aggregated Tau.

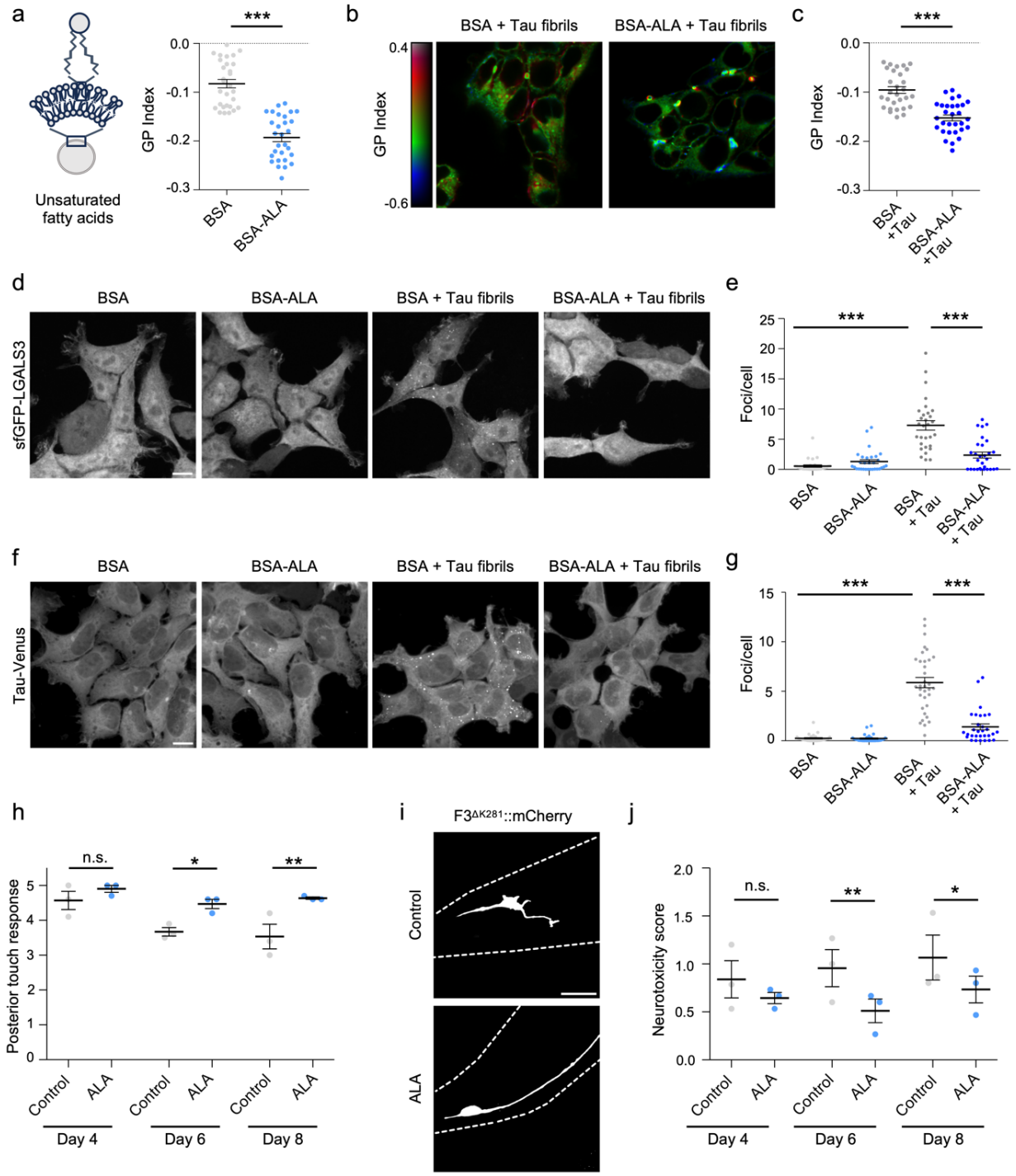

Figure 5: PUFA supplementation restores lysosomal membrane integrity and reduces seeded Tau aggregation and toxicity

a Left: unsaturated fatty acid membrane scheme. Right: C-Laurdan GP Index of HEK293T cells pre-loaded with 150 µM ALA conjugated to BSA (BSA-ALA) indicating an increase in membrane fluidity. Statistical analysis was done with a t-test. n= 3 independent experiments, 10 images each. **b** Pseudocolored HEK293T cells pre-loaded with BSA-ALA and seeded with 1N4R Tau fibrils. **c** GP Index indicates that BSA-ALA

387 reduces Tau-induced rigidification of the membrane. Statistical analysis was done using the Mann-Whitney
388 U-test. n= 3 independent experiments, 10 images each. **d** Max. intensity projection of confocal z-stacks of
389 HEK293T cells expressing sfGFP-LGALS3 pre-loaded with BSA-ALA and seeded with 1N4R Tau fibrils.
390 Scale bar 10 µm. **e** Quantification of sfGFP-LGALS3 foci following indicated treatments. n= 3 independent
391 experiments, 10 images each. **f** Max. intensity projection of confocal z-stacks of Tau-Venus biosensor cell
392 line pre-loaded with BSA-ALA and seeded with 1N4R Tau fibrils. Scale bar 10 µm. **g** Quantification of
393 Tau-Venus foci following indicated treatments. Statistical analysis comparing BSA + Tau to other
394 conditions was done using Kruskal-Wallis with Dunn's post-hoc test. n= 3 independent experiments, 10
395 images each. **h** Posterior response to touch during aging of animals expressing $F3^{\Delta K281}$::mCherry grown on
396 plates supplemented with ALA or only the ethanol solvent. Statistical analysis was done using two-way
397 ANOVA with Bonferroni's multiple comparison test. **i** Max. intensity projection of confocal z-stacks of
398 day 6 old animals expressing $F3^{\Delta K281}$::mCherry. **j** Neurotoxicity score of PLM neurons of animals grown
399 on control or ALA plates. Statistical analysis was done using 2-way ANOVA with a Holm-Sidak's multiple
400 comparison test. n= 3 independent experiments, 15 worms per replicate. Scale bar 20 µm. * = $p < 0.05$, **
401 = $p < 0.01$, *** = $p < 0.001$.

402 **Discussion**

403 In a previous genome-wide screen in *C. elegans*, we identified genes involved in SL
404 metabolism as crucial for endolysosomal integrity preservation[11]. In this study we explored the
405 mechanisms by which disruption of SL homeostasis leads to endolysosomal rupture and how it
406 affects Tau pathology. We found that imbalanced SL metabolism leads to decreased membrane
407 fluidity, and subsequent endolysosomal rupture. This promoted seeded Tau aggregation in a
408 biosensor cell line exposed to fibrillar Tau, implying that dysregulation of SL metabolism might
409 boost disease progression by enhancing propagation of Tau aggregation.

410 The central nervous system (CNS) is particularly rich in lipids. Approximately 50% of the
411 brain's dry weight consists of lipids with high concentrations of cholesterol, phospholipids and
412 sphingolipids[28,29]. Alterations in lipid and SL metabolism have been observed not only during the
413 aging process, but also in various late-onset neurodegenerative diseases including AD[15,30]. While
414 aging is the major risk factor for AD, one of the most significant genetic risk factors for AD is the
415 apolipoprotein E (ApoE) polymorphism, specifically the ApoE4 allele[31]. ApoE is the primary
416 lipoprotein in the brain, crucial for lipid transport and metabolism. Besides cholesterol, the ApoE4
417 variant has been shown to influence SL metabolism, thereby affecting the pathogenesis of AD
418 from its early stages[30,32]. While disturbances in SL homeostasis are increasingly recognized as a
419 contributing factor to the onset and progression of the disease[15,30], the underlying mechanisms are
420 poorly understood.

421 Our results show that reducing the expression of genes involved in both, biosynthesis and
422 degradation of SLs significantly reduced the fluidity of endolysosomal membranes, making them
423 more fragile and prone to rupture. KD of the saposin *spp-10*, the sphingosine kinase *sphk-1*, and
424 the sphingosine-1-phosphate lyase *spl-1* blocks the degradation of complex SLs and should lead
425 to an increase in their relative abundance, and therefore to a decrease in membrane fluidity. KD of
426 the very-long-chain (3R)-3-hydroxyacyl-CoA dehydratase *hpo-8*, which is involved in fatty acid
427 elongation, has been demonstrated to promote the incorporation of long-chain UFAs into
428 phospholipids, thereby restoring plasma membrane fluidity[33]. The absence of *hpo-8* leads to
429 membrane rigidification[33]. Conversely, KD of the serine incorporator *R11H6.*2 and the 3-
430 ketodihydrosphingosine reductase *Y37E11AM.3*, which function in the SL de novo synthesis
431 pathway, should theoretically decrease total SL content and consequently increase membrane
432 fluidity. The cytochrome b5 reductases *hpo-19* and *T05H4.4*, required for lipid desaturation, are

433 involved in the conversion of dihydroceramide to ceramide and the biosynthesis of PUFAs[34,35];
434 KD of these genes is expected to reduce the levels of SLs and PUFAs, which could theoretically
435 either increase or decrease membrane fluidity, depending on which metabolic pathway is
436 predominantly affected.

437 Our observation that KD of all these genes results in decreased membrane fluidity is
438 seemingly counterintuitive. However, SLs form a complex metabolic network and can
439 interconvert, allowing a dynamic adaptation of SL levels. In addition, the cell likely compensates
440 for the loss of certain SLs by increasing the biosynthesis of other lipid molecules. This dynamic
441 interplay makes it difficult to predict how individual genes affect the endolysosomal membrane
442 lipid composition. Genes that are involved in apparently opposing steps of SL metabolism could
443 therefore still lead to an accumulation of similar SL species. Future lipidomic analyses are
444 necessary to determine the SL and lipid content of endolysosomal membranes in our model
445 systems. Such studies will provide a clearer understanding of how genetic manipulation of SL
446 metabolism affects endomembrane lipid composition and could pinpoint the exact species likely
447 responsible for the observed membrane rigidification.

448 AD brains exhibit elevated levels of sphingosine, ceramide 1-phosphate, and ceramide
449 compared to control subjects[30]. Multivariate analysis and machine learning also identified these
450 SL species as key contributors to AD[30]. These and other analyses were performed in different brain
451 regions but without cell type or subcellular resolution. We found that disruption of *C. elegans* SL
452 homeostasis primarily affected endolysosomal membranes and had little effect on plasma
453 membrane fluidity. The lysosomal membrane is particularly rich in sphingolipids[36], which seems
454 to make it more susceptible to disruption of SL homeostasis. It would be important to examine
455 whether the observed changes in SL species in AD are primarily originating from endolysosomal
456 membranes or also from other organelles such as the endoplasmic reticulum or the cell membrane.
457 Intriguingly, expression of the aggregation-prone F3 Tau fragment also enhanced membrane
458 rigidity with SL homeostasis disruption having an additive effect, exacerbating endomembrane
459 damage. Thus, alterations in SL metabolism could be not only a cause but also a consequence of
460 AD related pathology[15,30]. The accumulation of misfolded Tau in lysosomes could impair the
461 lysosomal clearance capacity. This dysfunction may reduce the activity of acid hydrolases, leading
462 to an accumulation of biomolecules, including membrane lipids. Impairment of membrane lipid
463 metabolism could in turn further compromise lysosomal integrity and function. Both processes -

464 accumulation of SLs and protein aggregates - may create a vicious self-promoting cycle of
465 lysosomal dysfunction that eventually leads to neurodegeneration.

466 Supplementation of SFAs exacerbated the negative impact of the F3 Tau fragment on
467 endomembrane fluidity. Given the high levels of saturated and trans fats in the Western diet[37], it
468 is plausible that dietary factors also contribute to the dysregulation of lipid homeostasis in the
469 brain. The Mediterranean UFA-rich diet has been associated with healthy aging, while reduced
470 UFA brain levels have been correlated with increased Tau and Aβ pathology and decreased
471 cognitive function in AD[38]. Restoring membrane fluidity through the supplementation of PUFAs
472 mitigated Tau propagation in cells and reduced Tau-associated neurotoxicity in *C. elegans*. These
473 results suggest a potential mechanism for the beneficial effects of PUFA supplementation observed
474 in AD patients[39,40]. Future studies are needed to evaluate whether these benefits are related to an
475 increase in the fluidity of endolysosomal membranes and the consequent prevention of their
476 damage by protein aggregates and/or impaired SL homeostasis.

477 In sum, this study revealed an important role of endolysosomal membrane homeostasis in
478 disease progression providing a possible mechanism for the detrimental effect of SL imbalance
479 and beneficial effect of PUFA supplementation that have been observed in AD patients.

Acknowledgement

We gratefully acknowledge the technical support of Sarah Wübbel. We extend our gratitude to Dr. Sunil Yeruva for his assistance with the use of the DMI6000 confocal microscope. We appreciate the help of Dr. Hana Nuskova and Dr. Aurelio Teleman (DKFZ, Heidelberg) with the fatty acid conjugation protocol. The TauP301S-Venus expressing HEK293T cell line was kindly provided by Dr. William A. McEwan (Cambridge University)[26]. The pLenti PGK Puro DEST (w529-2) vector was a gift from Dr. Eric Campeau and Dr. Paul Kaufman[41]. We also thank Dr. Bin Liu and Dr. Marja Jäättelä (University of Copenhagen) for sharing the strain BIJ34 and a pPD49.26 expression plasmid coding for sfGFP::LGALS3 and Dr. Xiaochen Wang (Chinese Academy of Sciences, Beijing) for nematodes expressing the qxIs352 transgene. Some strains were provided by the Caenorhabditis Genetics Center (CGC), which is funded by the NIH Office of Research Infrastructure Programs (P40 OD010440). This work was supported by the Alzheimer Forschungs Initiative (AFI, grant #21053) (to CNK) and The Fondation pour la Recherche Médicale, contract ALZ201912009776 (to RM).

Competing interest statement

The authors declare no competing interest.

Author contribution

Conceptualization J.T., C.A.S., C.N.K.

Formal Analysis J.T., C.A.S., N.M.

Funding acquisition R.M., C.N.K.

Investigation J.T., C.A.S., N.M., D.E.

Methodology J.T., C.A.S., N.M.

Project administration C.N.K.

Resources S.B.N.N.

Supervision R.M., C.N.K.

Visualization J.T., C.N.K.

Writing – original draft J.T., C.A.S., C.N.K.

Writing – review & editing J.T., C.A.S., N.M., D.E., R.M., C.N.K.

511 **Methods**

512 **Maintenance of *C. elegans* and age synchronization**

513 All animals were cultured using standard methods[42]. If not otherwise indicated, worms were grown
514 on nematode growth medium (NGM) plates seeded with *E. coli* strain OP50 at 20 °C. For RNAi,
515 NGM medium were supplemented with Ampicillin, Tetracycline, and IPTG, seeded with the
516 respective HT115 *E. coli* RNAi clones and grown at 20 °C. Animals were age-synchronized by
517 bleaching. Briefly, gravid adults were dissolved in 20% sodium hypochlorite solution. The
518 surviving *C. elegans* embryos were hatched overnight in M9 buffer with gentle rocking at 20 °C.
519 The next day, appropriate amounts of L1 larvae were added to the plates.

520

521 ***C. elegans* fatty acid supplementation**

522 Polyunsaturated fatty acids were dissolved in EtOH and stored in the dark at -20 °C under a N_2
523 atmosphere to prevent oxidation. NGM was cooled after autoclaving to 55 °C. To enhance fatty
524 acid distribution, NP-40 substitute (0.001% v/v) was added to the media and subsequently either
525 0.3 mM of the desired fatty acid solution or the ethanol solvent as control and stirred for 5 min
526 before plate pouring[43]. Palmitic acid (PA) was supplemented by enriching the OP50 bacterial food
527 source. Overnight cultures were grown in the presence of 2 mM of PA dissolved in EtOH or EtOH.
528 The next day, OP50 bacteria were pelleted by centrifugation (10 min at 4500x g) and washed 2x
529 with M9 buffer[44]. 10x concentrated bacteria (in M9) were then seeded on NGM plates.

530

531 **Quantification of lysosomal rupture (galectin puncta assay) in *C. elegans***

532 Quantification of animals showing hypodermal lysosomal rupture was done as previously
533 described[16,45]. Briefly, age-synchronized animals expressing the sfGFP::LGALS3 construct in the
534 hypodermis were seeded on OP50 or RNAi NGM plates. Scoring was done using a Leica M205
535 FA widefield binocular microscope. 20-50 worms were analyzed per replicate.

536

537 **Mounting of live animals for imaging**

538 Synchronized animals were mounted on 8-10% agarose in M9 buffer pads with a drop of mounting
539 mix (2% (w/v) levamisole and 50% (v/v) nanosphere size standards (Thermo Fisher)) and covered
540 with a coverslip.

541

542 **Fluorescence recovery after photobleaching (FRAP)**

543 FRAP measurements to estimate membrane fluidity were done following a published protocol[46]
544 Animals were synchronized by bleaching and grown until the second day of adulthood on the
545 indicated RNAi or empty vector (EV) control plates. Directly before the FRAP experiments,
546 animals were mounted at the Zeiss LSM 780 confocal microscope. FRAP measurements of either
547 GFP enriched in the intestinal plasma membrane, or LAAT-1::mCherry located in intestinal or
548 hypodermal lysosomal membranes were taken with 40X Water immersion objective. For the
549 lysosomal membrane, mCherry-positive membranes were photobleached over a circular area
550 (seven pixel radius) using 10 iterations of the 561 nm DPSS laser with 100% laser power
551 transmission. Images were collected at a 12-bit intensity resolution over 128 × 128 pixels (digital
552 zoom 6X) using a pixel dwell time of 3.15 µsec with 2% laser power transmission. For the plasma
553 membrane, GFP-positive membranes were photobleached over a circular area (10 pixel radius)
554 using 20 iterations of the 488 nm Argon laser with 100% laser power transmission. Images were
555 collected at a 12-bit intensity resolution over 128 × 128 pixels (digital zoom 6X) using a pixel
556 dwell time of 3.15 µsec with 10% laser power transmission. At least 6 pre-bleaching images were
557 collected before the region of interest was bleached. The recovery of fluorescence was traced for
558 25s. Fluorescence recovery and T_{half} were calculated as previously described in Svensk et al.[47]
559

560 **Touch sensory assay and neurotoxicity in touch receptor neurons**

561 Touch sensory assay was done as described in[48]. Briefly, touch sensitivity was tested by gently
562 stroking the tip of an eyebrow hair attached to a toothpick transversely across the anterior or
563 posterior half of an animal. A touch-sensitive animal was one that stopped/moved away from the
564 stimulus. 10 worms were examined for each strain in 3 biological replicates with 5 strokes in the
565 anterior and posterior.

566 For neurotoxicity scoring of the PLM neurons, live animals were imaged using an Olympus
567 IXplore SpinSR Confocal microscope with an UplanS Apo 60x/1.30 Silicon oil objective. The
568 neurotoxicity score was determined by adding a score of 1 for each of the following phenotypes:
569 soma outgrowth, process branching, process break, wavy process. 15 animals were examined at
570 each day of age in 3 independent biological replicates.
571
572

573 **Cell culture**

574 Cells were cultured in DMEM containing high glucose, GlutaMAX Supplement, pyruvate (Gibco),
575 and 10% FBS (Gibco) at 37 °C and 5% CO_2. Regular mycoplasma tests were performed (GATC
576 Biotech). HEK293T cells expressing Venus-tagged full-length P301S mutant 0N4R Tau (0N4R
577 TauP301S-Venus) were kindly provided by Dr. William A. McEwan, Cambridge University[26].

578

579 **Cloning of mammalian expression constructs and generation of sfGFP-LGALS3 HEK293T**
580 **cells**

581 HEK293T cells were cultured in DMEM containing high glucose, GlutaMAX supplement,
582 pyruvate (Gibco), and 10% FBS (Gibco) at 37 °C and 5% CO_2. Cells expressing sfGFP-LGALS3
583 were generated as follows. sfGFP::LGALS3 was amplified from the *C. elegans* expression plasmid
584 pPD49.26 by PCR and cloned into the pLenti PGK Puro DEST (w529-2) vector backbone
585 (Addgene plasmid #19068) by MultiSite Gateway cloning according to the manufacturers
586 protocol. pLenti PGK Puro DEST (w529-2) was a gift from Eric Campeau & Paul Kaufman [41].
587 After each cloning step plasmids isolated from bacterial colonies grown on selective media were
588 extracted with the GenEluteTM Five-Minute Plasmid Miniprep Kit (Qiagen) and validated by
589 sequencing. HEK293T sfGFP-LGALS3 were generated using a 3rd generation lentiviral system.
590 Lentivirus was produced by transiently transfecting HEK293T cells with the pLenti PGK Puro
591 DEST, MDL-gagpol, RSV-REV and IVS-VSVG at a ratio of 5:3:1:1, respectively. Cell media was
592 changed 24 hours after transfection. Viral supernatant was collected 72 h post-transfection. After
593 centrifugation at 2000 x g for 5 min, the supernatant containing the virus was concentrated by
594 adding the PEG-it Virus Precipitation Solution (Systems Biosciences) followed by overnight
595 incubation at 4 °C. The precipitated virus was pelleted by centrifugation (1500 x g, 30 min, 4°C),
596 resuspended in DMEM containing 25 mM HEPES buffer and stored at -80 °C. The lentivirus was
597 added to HEK293T followed by treatment with Puromycin to select successfully transduced
598 HEK293T cells stably expressing sfGFP-LGALS3.

599

600 **Quantification of lysosomal rupture (galectin puncta assay) in cells**

601 Cells were imaged on an Olympus IXplore SpinSR Confocal microscope with an UplanS Apo
602 60x/1.30 Silicon oil objective. To detect the number of foci in an image, a difference of gaussian
603 blur was applied to max projections to isolate foci from cytsosolic sfGFP signal. Thresholding was

604 applied using 'moments' threshold on FIJI. Number of foci was counted using the 'analyze
605 particles' function. Cell number was counted manually to obtain number of foci/cell for each
606 image.
607
608 **C-Laurdan dye measurement of membrane fluidity in worms and cells**
609 Live worms were stained with 10 mM C-Laurdan dye (6-dodecanoyl-2-
610 dimethylaminonaphthalene) (Thermo Fisher Scientific) as previously described in[49]. Cells were
611 also stained with C-Laurdan at 15 µM for 2 hours then fixed in 4% PFA in PBS. Images were
612 acquired with an DMI6000 confocal microscope and Leica software with a 63x oil-immersion
613 objective, with a zoom factor of 4. Samples were excited with a 405 nm laser and the emission
614 recorded between 400 and 460 nm (ordered phase) and between 470 and 530 nm (disordered
615 phase). Quantitative assessment of the membrane order was achieved by calculating the ratiometric
616 relationship of the fluorescence intensity recorded in two spectral channels (GP value) by using an
617 automated ImageJ macro, according to published guidelines[23]
618
619 **Knockdown of target genes by RNAi in cells**
620 SPHK2 or a scrambled control siRNA was purchased from Thermo Scientific Dharmacon
621 (ONTarget plus siRNA and Control Pool). Cells were seeded in DMEM with 10% FBS. siRNA
622 was diluted in siRNA buffer (Final concentration 20 nM) before mixing with Lipofectmine2000
623 for 20 min prior to being added to cells. To minimize lipofectamine impact on the endolysosomal
624 system, media was exchanged after 6 hours.
625
626 **SDS-Page and immunoblotting**
627 Cells were pelleted by centrifugation followed by lysis in lysis buffer (10mM Tris, 100mM NaCl,
628 0.2% Triton X-100, 10mM EDTA) on ice for 20 min. The lysates were transferred into fresh
629 Eppendorf tubes and centrifuged (1000 g for 1 min at 4 °C) in a tabletop centrifuge to remove
630 cellular debris. The protein concentration was determined using protein assay dye reagent
631 concentrate (Bio-Rad). Proteins were separated under denaturing conditions by SDS–PAGE and
632 transferred onto a PVDF membrane (Carl Roth) by standard wet blotting protocols. Samples were
633 probed with rabbit polyclonal anti-SPHK2 (1:5000, 9C5E1, Santa Cruz) primary antibody. Anti-
634 GAPDH antibody (1:5000, clone GAPDH-71.1, Sigma-Aldrich) was used as loading control.

635 HRP-conjugated anti-mouse and anti-rabbit IgG secondary antibodies (Bio-Rad) were used for
636 subsequent ECL-based detection (Bio-Rad).
637
638 **Fatty acid treatment in cells**
639 For α-linolenic acid (ALA), a stock solution was made in EtOH and stored in the dark at -20°C
640 under a N_2 atmosphere to prevent oxidation[50]. Palmitic acid (PA) was dissolved in 0.1 M NaOH
641 according to[51]. ALA and PA were then conjugated to BSA in 10% fatty acid free solution by
642 shaking for 1 hour at 37°C to a concentration of 6 mM for ALA and 5 mM for PA[52]. Prior to
643 preloaded cells with BSA-PA, the solution was heated to 65 °C for 15 min. For assays with C-
644 Laurdan, cells were preloaded with FAs for 3 hours before the addition of C-Laurdan for another
645 2 hours. If preloading was followed by seeding with Tau, preloading with FAs was done for 3
646 hours before fibrillar Tau was added for an additional 5 hours. C-Laurdan was spiked in for the
647 last 2 hours. No media changes were done between steps. For experiments with HEK293T Tau-
648 Venus cells and HEK293T sfGFP-LGALS3 cells, preloading with FAs was done for 3 hours before
649 seeding with 1N4R Tau fibrils. Cells were then fixed after 48 hours.
650
651 **Monomeric and fibrillar Tau**
652 Full-length human 1N4R Tau was expressed and purified as previously described[53]. The purified
653 monomeric Tau was dialyzed against PBS buffer containing 1 mM DTT, flash frozen in liquid
654 nitrogen and stored at -80 °C. The concentration of monomeric Tau was determined
655 spectrophotometrically using an extinction coefficient at 280 nm of 7575 M^{-1} cm^{-1}. Monomeric
656 1N4R Tau was assembled into fibrils at 40 μM in the presence of 10 μM heparin, in PBS buffer
657 containing 1 mM DTT under continuous shaking (600 rpm) for 5 days at 37 °C in an Eppendorf
658 Thermomixer. The quality of 1N4R Tau fibrils produced after 5 days was assessed by ThioflavinT
659 binding, sedimentation, and transmission electron microscopy (TEM).
660 The resulting 1N4R Tau fibrils were spun at 25 °C and 75 000 g for 30 min. The pelleted fibrils
661 were resuspended in PBS buffer with 1 mM DTT at 50 μM equivalent monomeric Tau
662 concentration. 1N4R Tau fibrils were labeled by incubation with the 2 molar equivalents of lysine-
663 reactive ATTO 550 (ATTO-TEC, GMBH) for 1 h at room temperature. The unreacted fluorophore
664 was removed by two cycles of centrifugation at 75 000 g for 10 min and resuspension of the pellet
665 in PBS. 1N4R Tau fibrils were fragmented by sonication for 5 min in 2-ml Eppendorf tubes in a

666 Vial Tweeter powered by an ultrasonic processor UIS250v (250 W, 2.4 kHz; Hielscher Ultrasonic,
667 Teltow, Germany) to generate fibrillar particles with an average size 50 nm as assessed by TEM
668 analysis. For seeding experiments, either monomeric or fibrillar Tau was added directly into the
669 cell culture media to a final concentration of 400 nM. Cells were then fixed after 48 hours.
670
671 **Statistical analysis**
672 Statistical analysis was performed with GraphPad Prism (GraphPad Software, Version 6h and
673 10.1.1). Data was tested for normal distribution by D'Agostino and Pearson omnibus normality
674 test. Data presentation, sample size (number of biological repeats and sample size per repeat and
675 condition), and the applied statistical tests are indicated in the figure legends for each experiment.
676 For all cell culture data, data represents 3 independent replicates with 10 images each replicate.
677 Significance levels: non-significant (n.s.) $p > 0.05$, $*p \leq 0.05$, $**p \leq 0.01$, and $***p \leq 0.001$.
678

References

1. Clavaguera, F. *et al.* Transmission and spreading of tauopathy in transgenic mouse brain. *Nat Cell Biol* **11**, 909 (2009).
2. Rösler, T. W. *et al.* Four-repeat tauopathies. *Prog Neurobiol* **180**, 101644 (2019).
3. Caballero, B. *et al.* Interplay of pathogenic forms of human tau with different autophagic pathways. *Aging Cell* **17**, e12692 (2018).
4. Lim, F. *et al.* FTDP-17 mutations in tau transgenic mice provoke lysosomal abnormalities and Tau filaments in forebrain. *Mol Cell Neurosci* **18**, 702–714 (2001).
5. Menzies, F. M., Fleming, A. & Rubinsztein, D. C. Compromised autophagy and neurodegenerative diseases. *Nat Rev Neurosci* **16**, 345–357 (2015).
6. Piovesana, E. *et al.* Tau accumulation in degradative organelles is associated to lysosomal stress. *Scientific Reports 2023 13:1* **13**, 1–14 (2023).
7. Caballero, B. *et al.* Acetylated tau inhibits chaperone-mediated autophagy and promotes tau pathology propagation in mice. *Nature Communications 2021 12:1* **12**, 1–18 (2021).
8. Chen, J. J. *et al.* Compromised function of the ESCRT pathway promotes endolysosomal escape of tau seeds and propagation of tau aggregation. *J Biol Chem* **294**, 18952–18966 (2019).
9. Flavin, W. P. *et al.* Endocytic vesicle rupture is a conserved mechanism of cellular invasion by amyloid proteins. *Acta Neuropathol* **134**, 629–653 (2017).
10. Rose, K. *et al.* Tau fibrils induce nanoscale membrane damage and nucleate cytosolic tau at lysosomes. *Proceedings of the National Academy of Sciences* **121**, e2315690121 (2024).
11. Sandhof, C. A. *et al.* A Novel C. elegans Model for Tau Spreading Reveals Genes Critical for Endolysosomal Integrity and Seeded Tau Aggregation. *BioRxiv* (2024).
12. Breslow, D. K. & Weissman, J. S. Membranes in Balance: Mechanisms of Sphingolipid Homeostasis. *Mol Cell* **40**, 267 (2010).
13. Gault, C. R., Obeid, L. M. & Hannun, Y. A. An overview of sphingolipid metabolism: from synthesis to breakdown. *Adv Exp Med Biol* **688**, 1 (2010).
14. Czubowicz, K., Jęśko, H., Wencel, P., Lukiw, W. J. & Strosznajder, R. P. The Role of Ceramide and Sphingosine-1-Phosphate in Alzheimer's Disease and Other Neurodegenerative Disorders. *Mol Neurobiol* **56**, 5436–5455 (2019).
15. Van Echten-Deckert, G. & Walter, J. Sphingolipids: Critical players in Alzheimer's disease. *Prog Lipid Res* **51**, 378–393 (2012).
16. Aits, S. *et al.* Sensitive detection of lysosomal membrane permeabilization by lysosomal galectin puncta assay. *Autophagy* **11**, 1408–1424 (2015).
17. Kanehisa, M. & Goto, S. KEGG: Kyoto Encyclopedia of Genes and Genomes. *Nucleic Acids Res* **28**, 27 (2000).
18. Hänel, V., Pendleton, C. & Witting, M. The sphingolipidome of the model organism Caenorhabditis elegans. *Chem Phys Lipids* **222**, 15–22 (2019).
19. Cheng, X. *et al.* Sphingolipidomic Analysis of C. elegans reveals Development- and Environment-dependent Metabolic Features. *Int J Biol Sci* **15**, 2897–2910 (2019).
20. D'Auria, L. & Bongarzone, E. R. THE FLUID LEVITY OF THE CELL: THE ROLE OF MEMBRANE LIPID ARCHITECTURE IN GENETIC SPHINGOLIPIDOSES. *J Neurosci Res* **94**, 1019 (2016).

723 21. Liu, B., Du, H., Rutkowski, R., Gartner, A. & Wang, X. LAAT-1 is the Lysosomal
724 Lysine/Arginine Transporter that Maintains Amino Acid Homeostasis. *Science* **337**, 351
725 (2012).
726 22. Mörck, C. *et al.* Statins inhibit protein lipidation and induce the unfolded protein response
727 in the non-sterol producing nematode Caenorhabditis elegans. *Proc Natl Acad Sci U S A*
728 **106**, 18285 (2009).
729 23. Owen, D. M., Rentero, C., Magenau, A., Abu-Siniyeh, A. & Gaus, K. Quantitative
730 imaging of membrane lipid order in cells and organisms. *Nature Protocols 2012 7:1* **7**,
731 24–35 (2011).
732 24. Barucha-Kraszewska, J., Kraszewski, S. & Ramseyer, C. Will C-Laurdan dethrone
733 Laurdan in fluorescent solvent relaxation techniques for lipid membrane studies?
734 *Langmuir* **29**, 1174–1182 (2013).
735 25. Wittrup, A. *et al.* Visualizing lipid-formulated siRNA release from endosomes and target
736 gene knockdown. *Nat Biotechnol* **33**, 870 (2015).
737 26. McEwan, W. A. *et al.* Cytosolic Fc receptor TRIM21 inhibits seeded tau aggregation.
738 *Proc Natl Acad Sci U S A* **114**, 574–579 (2017).
739 27. Nachman, E. *et al.* Disassembly of Tau fibrils by the human Hsp70 disaggregation
740 machinery generates small seeding-competent species. *Journal of Biological Chemistry*
741 jbc.RA120.013478 (2020) doi:10.1074/jbc.RA120.013478.
742 28. Yoon, J. H. *et al.* Brain lipidomics: From functional landscape to clinical significance. *Sci*
743 *Adv* **8**, 9317 (2022).
744 29. Hornemann, T. Mini review: Lipids in Peripheral Nerve Disorders. *Neurosci Lett* **740**,
745 (2021).
746 30. Uranbileg, B. *et al.* Alzheimer's disease manifests abnormal sphingolipid metabolism.
747 *Front Aging Neurosci* **16**, 1368839 (2024).
748 31. Corder, E. H. *et al.* Gene dose of apolipoprotein E type 4 allele and the risk of
749 Alzheimer's disease in late onset families. *Science* **261**, 921–923 (1993).
750 32. Kosicek, M., Zetterberg, H., Andreasen, N., Peter-Katalinic, J. & Hecimovic, S. Elevated
751 cerebrospinal fluid sphingomyelin levels in prodromal Alzheimer's disease. *Neurosci Lett*
752 **516**, 302–305 (2012).
753 33. Ruiz, M. *et al.* AdipoR2 recruits protein interactors to promote fatty acid elongation and
754 membrane fluidity. *Journal of Biological Chemistry* **299**, (2023).
755 34. Zhang, Y. *et al.* The cytochrome b5 reductase HPO-19 is required for biosynthesis of
756 polyunsaturated fatty acids in Caenorhabditis elegans. *Biochimica et Biophysica Acta*
757 *(BBA) - Molecular and Cell Biology of Lipids* **1861**, 310–319 (2016).
758 35. Casasampere, M., Ordoñez, Y. F., Pou, A. & Casas, J. Inhibitors of dihydroceramide
759 desaturase 1: Therapeutic agents and pharmacological tools to decipher the role of
760 dihydroceramides in cell biology. *Chem Phys Lipids* **197**, 33–44 (2016).
761 36. Fabri, J. H. T. M., de Sá, N. P., Malavazi, I. & Del Poeta, M. The dynamics and role of
762 sphingolipids in eukaryotic organisms upon thermal adaptation. *Prog Lipid Res* **80**,
763 101063 (2020).
764 37. Rakhra, V., Galappaththy, S. L., Bulchandani, S. & Cabandugama, P. K. Obesity and the
765 Western Diet: How We Got Here. *Mo Med* **117**, 536 (2020).
766 38. Snowden, S. G. *et al.* Association between fatty acid metabolism in the brain and
767 Alzheimer disease neuropathology and cognitive performance: A nontargeted
768 metabolomic study. *PLoS Med* **14**, (2017).

39. Shinto, L. *et al.* A Randomized Placebo-Controlled Pilot Trial of Omega-3 Fatty Acids and Alpha Lipoic Acid in Alzheimer's Disease. *J Alzheimers Dis* **38**, 111–120 (2014).
40. Wood, A. H. R., Chappell, H. F. & Zulyniak, M. A. Dietary and supplemental long-chain omega-3 fatty acids as moderators of cognitive impairment and Alzheimer's disease. *Eur J Nutr* **61**, 589 (2022).
41. Campeau, E. *et al.* A versatile viral system for expression and depletion of proteins in mammalian cells. *PLoS One* **4**, (2009).
42. Brenner, S. The Genetics of CAENORHABDITIS ELEGANS. *Genetics* **77**, 71 (1974).
43. Svensk, E. *et al.* PAQR-2 Regulates Fatty Acid Desaturation during Cold Adaptation in C. elegans. *PLoS Genet* **9**, e1003801 (2013).
44. Devkota, R. *et al.* The adiponectin receptor AdipoR2 and its Caenorhabditis elegans homolog PAQR-2 prevent membrane rigidification by exogenous saturated fatty acids. *PLoS Genet* **13**, e1007004 (2017).
45. Sandhof, C. A. *et al.* Reducing INS-IGF1 signaling protects against non-cell autonomous vesicle rupture caused by SNCA spreading. *Autophagy* **16**, 878–899 (2020).
46. Devkota, R. & Pilon, M. FRAP: A Powerful Method to Evaluate Membrane Fluidity in Caenorhabditis elegans. *Bio Protoc* **8**, (2018).
47. Svensk, E. *et al.* Caenorhabditis elegans PAQR-2 and IGLR-2 Protect against Glucose Toxicity by Modulating Membrane Lipid Composition. *PLoS Genet* **12**, e1005982 (2016).
48. Chalfie, M. *et al.* The neural circuit for touch sensitivity in Caenorhabditis elegans. *The Journal of Neuroscience* **5**, 956 (1985).
49. Jeong, J. H. *et al.* A new AMPK isoform mediates glucose-restriction induced longevity non-cell autonomously by promoting membrane fluidity. *Nature Communications 2023 14:1* **14**, 1–17 (2023).
50. Oliveira, A. F. *et al.* In vitro use of free fatty acids bound to albumin: A comparison of protocols. *Biotechniques* **58**, 228–233 (2015).
51. Cousin, S. P. *et al.* Free Fatty Acid-Induced Inhibition of Glucose and Insulin-Like Growth Factor I-Induced Deoxyribonucleic Acid Synthesis in the Pancreatic β-Cell Line INS-1*This work was supported by grants from the NIH (GK-55267), the Juvenile Diabetes Foundation International, the German Research Society, and BetaGene, Inc. *Endocrinology* **142**, 229–240 (2001).
52. Nůsková, H. *et al.* Competition for cysteine acylation by C16:0 and C18:0 derived lipids is a global phenomenon in the proteome. *Journal of Biological Chemistry* **299**, 105088 (2023).
53. Tardivel, M. *et al.* Tunneling nanotube (TNT)-mediated neuron-to neuron transfer of pathological Tau protein assemblies. *Acta Neuropathol Commun* **4**, 117 (2016).
54. Chitwood, D. J., Lusby, W. R., Thompson, M. J., Kochansky, J. P. & Howarth, O. W. The glycosylceramides of the nematode Caenorhabditis elegans contain an unusual, branched-chain sphingoid base. *Lipids* **30**, 567–573 (1995).
55. Zhang, H. *et al.* Apicobasal domain identities of expanding tubular membranes depend on glycosphingolipid biosynthesis. *Nature Cell Biology 2011 13:10* **13**, 1189–1201 (2011).
56. Zhu, H., Shen, H., Sewell, A. K., Kniazeva, M. & Han, M. A novel sphingolipid-TORC1 pathway critically promotes postembryonic development in Caenorhabditis elegans. *Elife* **2013**, (2013).

813 57. Scholz, J., Helmer, P. O., Nicolai, M. M., Bornhorst, J. & Hayen, H. Profiling of
814 sphingolipids in Caenorhabditis elegans by two-dimensional multiple heart-cut liquid
815 chromatography – mass spectrometry. *J Chromatogr A* **1655**, 462481 (2021).
816
817